ELSEVIER

Polymer 43 (2002) 3025–3033

polymer

www.elsevier.com/locate/polymer

Polymer chains in semidilute solutions confined to a square channel: mean-field Gaussian chain theory and comparison with simulation results

Iwao Teraoka[a,*], Peter Cifra[b]

[a]Herman F. Mark Polymer Research Institute, Polytechnic University, 333 Jay Street, Brooklyn, NY 11201, USA
[b]Slovak Academy of Sciences, Polymer Institute, Dúbravská cesta 9, 842 36 Bratislava, Slovak Republic

Received 2 October 2001; accepted 22 January 2002

Abstract

We extend the mean-field Gaussian chain theory, originally developed for non-dilute solutions of athermal polymer chains in a slit, to solutions in a channel with a square cross section. The formulation allows one to calculate the monomer density profile, the chemical potential of the confined polymer chain, and therefore the partition coefficient. For the mean-field potential, we used the first-order approximation that neglects local monomer density fluctuations and the second-order approximation that takes into account the fluctuations. The results of the density profile and the partition coefficient were compared with those obtained in the lattice Monte Carlo simulations. The theoretical results obtained with the first-order approximation agreed well with the simulation results for chains of 100 beads below the average monomer density of ca. 0.2. At higher concentrations, the second-order results gave a better agreement. This cross over indicates a change in the interactions between polymer chains from those in one-dimension to those in three-dimensions as the correlation length in the confined solution becomes sufficiently shorter than the channel width. © 2002 Elsevier Science Ltd. All rights reserved.

Keywords: Partitioning; Confinement; Semidilute solutions

1. Introduction

Theoretical formulation for polymer chains in non-dilute solutions in a confining geometry had been limited to the scaling theory [1,2] until the Landau–Ginzburg free energy functional approach was taken by Brazhnik et al. [3]. Recently Teraoka and Wang [4] formulated the thermodynamics of an athermal polymer solution confined to a slit using a mean-field Gaussian chain theory. The mean-field potential in which a chain with a Gaussian conformation grows was determined so that, in the absence of the confinement, the Green function for the chain reproduces the dependence of the osmotic pressure on the polymer concentration for the bulk solutions obtained in the renormalization group theory [5,6]. We employed two levels of approximation for the mean-field potential. The first-order potential was obtained for a uniform monomer density in the bulk solution, and the second-order potential was calculated by taking into account the fluctuations in the local monomer density. Within the slit, the potential was defined at every point as a function of the mean local monomer density at that point. To account for the difference in the confinement entropy between the athermal chains and Gaussian chains, a Gaussian-equivalent radius of gyration R_{gG} was introduced; The Gaussian chain of R_{gG} and the real chain of R_g have the same confinement entropy in the slit. The formulation, applied to the Gaussian chain of R_{gG}, allowed calculation of the monomer density profile, the chain dimension across the slit, the chemical potential of the polymer chain, and therefore the partition coefficient. Use of the second-order mean-field potential achieved a good agreement between the theoretical prediction and the simulation results, especially in the monomer density profile and the partition coefficient [4]. Subsequently, we extended the theoretical formulation to the non-dilute polymer solutions in the theta condition confined to a slit [7]. The missing second virial coefficient made the weak-to-strong transition occur at much higher concentrations compared with the good solvent condition.

We recently studied the thermodynamics of polymer chains confined to a channel of a square cross section using lattice Monte Carlo simulations [8]. The concentration ranged from dilute to semidilute. At low concentrations, the partition coefficient K in the channel was close to, but slightly smaller than, the square of the partition coefficient K_s in the slit of the same wall-to-wall distance d. In the semidilute solution, whether the relationship $K \cong K_s^2$

---

* Corresponding author. Tel.: +1-718-260-3466; fax: +1-718-260-3125.
E-mail address: teraoka@poly.edu (I. Teraoka).

0032-3861/02/$ - see front matter © 2002 Elsevier Science Ltd. All rights reserved.
PII: S0032-3861(02)00098-8

holds compared at the same concentration in the surrounding solution equilibrated with the confined solutions was different between the weak confinement (the radius of gyration $\ll d$) and the strong confinement. In the weak confinement, $K \cong K_s^2$ holds in the whole concentration range. In the strong confinement, $K < K_s^2$ in the semidilute solution (the concentration refers to the one in the surrounding solution), but $K \cong K_s^2$ when the correlation length was sufficiently smaller than d.

The present work extends the theory [4] for the confined non-dilute athermal chains to the channel geometry. Now the confinement is in two directions. Except in the low concentration limit, the Green function is not independent between the two directions even for the mean-field Gaussian chain. We solve the problem by expanding the Green function in terms of two-dimensional eigenfunctions. A stronger confinement by the channel brings about a more prominent change in the thermodynamics compared with the slit geometry. We compare the theoretical results with those obtained in our lattice Monte Carlo simulations. The comparison will show that the partition coefficient and the density profile in the channel sensitively reflect the interactions between polymer chains.

2. Mean-field Gaussian chain theory

2.1. Review of Green function formulation for a single chain confined to a square channel

First, we review a Green function formulation for a single Gaussian chain [2,9]. The chain consists of N segments of length b. The Green function $G(\mathbf{r}, \mathbf{r}'; n)$, which is equal to the probability density of finding the nth segment at $\mathbf{r}$ when the 0th segment is at $\mathbf{r}'$, satisfies the following equation:

$$[\partial/\partial n - (b^2/6)\nabla^2 + U(\mathbf{r})]G(\mathbf{r},\mathbf{r}';n) = \delta(\mathbf{r}-\mathbf{r}')\delta(n) \quad (1)$$

where $0 \le n \le N$ and $U(\mathbf{r})$ is the potential energy reduced by thermal energy k_BT. When $U = 0$, it is explicitly given as:

$$G_0(\mathbf{r},\mathbf{r}';n) = (2\pi nb^2/3)^{-3/2}\exp[-3(\mathbf{r}-\mathbf{r}')^2/(2nb^2)] \quad (2)$$

For a single Gaussian chain trapped in a channel of square cross section of $d \times d$, i.e. $U(\mathbf{r}) = U(x,y) = 0$ $(0 < x, y < d)$ and ∞ (otherwise), the x and y components of the Green function are mutually independent. The z component does not change. The x component changes to

$$G_{0x}(x,x';n) = \sum_{k=1}^{\infty} u_{0k}(x)u_{0k}(x')\exp(-n\epsilon_{0k}) \quad (3)$$

where the normalized eigenfunctions

$$u_{0k}(x) = (2/d)^{1/2}\sin(k\pi x/d) \qquad (k = 1,2,\ldots) \quad (4)$$

and the eigenvalues

$$\epsilon_{0k} = (b^2/6)(k\pi/d)^2 \quad (5)$$

satisfy the eigenequation:

$$[-(b^2/6)\mathrm{d}^2/\mathrm{d}x^2 + U(x)]u_{0k}(x) = \epsilon_{0k}u_{0k}(x) \quad (6)$$

The y component $G_{0y}(y,y';n)$ experiences the same change.

The partition coefficient is defined as the ratio of the polymer concentration in the channel to that in the bulk solution when the two solutions are equilibrated with each other. The coefficient K_0 in the dilute solution limit is obtained as the probability of growing the whole chain without touching the channel walls starting at an arbitrary point within the channel. Integration of $G_{0x}(x,x';N)G_{0y}(y,y';N)$ with respect to x and y and then averaging with respect to x' and y' gives K_0 as:

$$K_0 = \left[\frac{8}{\pi^2}\sum_{k:\mathrm{odd}}^{\infty} k^{-2}\exp(-N\epsilon_{0k})\right]^2$$
$$= \left[\frac{8}{\pi^2}\sum_{k:\mathrm{odd}}^{\infty} k^{-2}\exp[-(k\pi R_{g0}/d)^2]\right]^2 \quad (7)$$

where $R_{g0}^2 = Nb^2/6$ is the mean square radius of gyration in the dilute bulk solution. In the low concentration limit, the partition coefficient with the channel of a cross section d^2 is equal to the square of the partition coefficient with the slit of width d. As in the slit geometry, the confinement entropy, $-k_B\ln K_0$, in the channel is determined by R_{g0}/d only, where k_B is the Boltzmann constant. It is twice as large as that in the slit.

2.2. Many-chain system confined to a square channel

In the square channel, the monomer density is high at the center and trails off toward the walls and the corners. We pay attention to the z-averaged Green function $G_{xy}(x,y;x',y';n)$ defined as $G_{xy}(x,y;x',y';n) \equiv \int \mathrm{d}z\, G(\mathbf{r},\mathbf{r}';n)$. It satisfies

$$\left[\frac{\partial}{\partial n} - \frac{b^2}{6}\left(\frac{\partial^2}{\partial x^2} + \frac{\partial^2}{\partial y^2}\right) + U(x,y)\right]G_{xy}(x,y;x',y';n)$$
$$= \delta(x-x')\delta(y-y')\delta(n) \quad (8)$$

We employ the mean-field potential $U(x,y) = N^{-1}f_m(\phi(x,y))$, where the monomer density $\phi(x,y)$ determines $U(x,y)$ in $0 < x, y < d$ and $U(x,y) = \infty$ otherwise.

The solution of Eq. (8) can be expressed just as G_{0x} in Eq. (3) as:

$$G_{xy}(x,y;x',y';n) = \sum_{k,l=1}^{\infty} u_{kl}(x,y)u_{kl}(x',y')\exp(-n\epsilon_{kl}) \quad (9)$$

where the eigenfunction $u_{kl}(x,y)$ is expressed by a Fourier series:

$$u_{kl}(x,y) = \sum_{i,j=1}^{\infty} a_{klij}u_{0i}(x)u_{0j}(y) \qquad (k,l = 1,2,\ldots) \quad (10)$$

with a_{klij} being the superposition coefficients. When $f_m = 0$ (at $\phi = 0$), $a_{klij} = \delta_{ki}\delta_{lj}$ and $\epsilon_{kl} = \epsilon_{0k} + \epsilon_{0l}$ with δ_{ij} being the Kronecker's delta. Then $G_{xy}(x,y;x',y';n)$ reduces to $G_{0x}(x,x';n)G_{0y}(y,y';n)$.

The eigenequation is now represented in the matrix form:

$$\mathbf{M}\mathbf{a}_{kl} = (N\epsilon_{kl})\mathbf{a}_{kl} \tag{11}$$

where $\mathbf{a}_{kl}$ is the transpose of $[a_{kl11}, a_{kl12}, \ldots]$, and the elements of $\mathbf{M}$ are given as:

$$M_{iji'j'} = N(\epsilon_{0i} + \epsilon_{0j})\delta_{ii'}\delta_{jj'} + U_{iji'j'} \qquad (i,j,i',j' = 1,2,\ldots) \tag{12}$$

where

$$U_{iji'j'} = \int_0^d \int_0^d u_{0i}(x)u_{0j}(y)f(\phi(x,y))u_{0i'}(x)u_{0j'}(y)\mathrm{d}x\,\mathrm{d}y \tag{13}$$

Symmetricity of $\phi(x,y)$ with respect to x, $y = d/2$ leads to $U_{iji'j'} = 0$ if i and i' have a different parity or j and j' have a different parity. Then from Eqs. (11) and (12), we find that $a_{klij} = 0$ if k and i have a different parity or l and j have a different parity. The matrix form of the eigenequation can be solved separately for $(k,l) =$ (odd, odd), (odd, even), (even, odd), and (even, even). The eigenequation for $(k,l) =$ (odd, odd) needs to be solved self-consistently, because $\phi(x)$ is determined by a_{klij} of odd k and l as shown below. The other eigenequations can be solved once $\phi(x)$ is determined.

The monomer density profile $\phi(x,y)$ at (x,y) is proportional to the probability of growing two partial chains of lengths n and $N-n$ from (x,y) in the given potential field, averaged with respect to n. It is expressed as:

$$\phi(x,y) \equiv p^{-1}\phi_{\mathrm{AV}} \int_0^d \mathrm{d}x' \int_0^d \mathrm{d}x'' \int_0^d \mathrm{d}y' \int_0^d \mathrm{d}y'' N^{-1} \int_0^N \mathrm{d}n \times G_{xy}(x',y';x,y;N-n)G_{xy}(x,y;x'',y'';n), \tag{14}$$

where $\phi_{\mathrm{AV}} = d^{-2}\int_0^d \int_0^d \phi(x,y)\mathrm{d}x\,\mathrm{d}y$ is the average density in the channel. The normalization requires p^{-1} with p being the insertion probability of the whole chain in the channel:

$$p = d^{-2}\int_0^d \mathrm{d}x' \int_0^d \mathrm{d}x'' \int_0^d \mathrm{d}y' \int_0^d \mathrm{d}y'' G_{xy}(x',y';x'',y'';N) = (8/\pi^2)^2 \sum_{k,l:\mathrm{odd}} b_{kl}^2 \exp(-N\epsilon_{kl}) \tag{15}$$

and

$$b_{kl} = \sum_{i,j:\mathrm{odd}} (i\,j)^{-1} a_{klij} \tag{16}$$

In the dilute solution limit, $b_{kl} = 1/(kl)$ and therefore $p = K_0$. At finite concentrations, however, the insertion probability is smaller than unity in the bulk solution as well, and therefore p is not equal to the partition coefficient any more.

In terms of a_{klij}, $\phi(x,y)$ is expressed as:

$$\phi(x,y) = \frac{\phi_{\mathrm{AV}}}{p}\left(\frac{8d}{\pi^2}\right)^2 \sum_{j,m:\mathrm{odd}} \sum_{j',m':\mathrm{odd}} c_{jmj'm'} u_{0j}(x)u_{0m}(y)u_{0j'}(x)u_{0m'}(y) \tag{17}$$

where

$$c_{jmj'm'} = \sum_{k,l:\mathrm{odd}} b_{kl}a_{kljm} \sum_{k',l':\mathrm{odd}} b_{k'l'}a_{k'l'j'm'}e_{klk'l'} \tag{18}$$

with

$$e_{klk'l'} = \begin{cases} \exp(-N\epsilon_{kl}) & (k,l) = (k',l') \\ \dfrac{\exp(-N\epsilon_{k'l'}) - \exp(-N\epsilon_{kl})}{N(\epsilon_{kl} - \epsilon_{k'l'})} & (k,l) \neq (k',l') \end{cases} \tag{19}$$

To implement the eigenequation into a computer program, the dual index (k,l) in Eq. (11) was coded into a one-dimensional index. Now $\mathbf{M}$ is a regular two-dimensional matrix and $\mathbf{a}_{kl}$ a vector. Other equations also benefit from this encoding. The Appendix A explains details of the computation method.

2.3. Mean-field potentials, unperturbed eigenvalues, and chemical potentials

For the mean-field potential f_{m}, we employ the first- and second-order approximations. The two potential functions f_{m1} and f_{m2} are respectively given as [4]:

$$f_{\mathrm{m1}}(\phi) = P(\phi) - 1 + \int_0^{\phi} [P(\varphi) - 1]\varphi^{-1}\,\mathrm{d}\varphi \tag{20}$$

$$f_{\mathrm{m2}}(\phi) = f_{\mathrm{m1}}(\phi) + \ln[\cosh h(\phi)] \tag{21}$$

with

$$h(\phi) = f'_{\mathrm{m1}}(\phi)\langle\Delta\phi(\mathbf{r}_1)\Delta\phi(\mathbf{r}_2)\rangle \tag{22}$$

where the prime denotes the derivative. The first-order approximation assumes a uniform monomer density throughout the system to derive the potential function. The second-order approximation takes into account the pair correlation in the local monomer density fluctuations, $\langle\Delta\phi(\mathbf{r}_1)\Delta\phi(\mathbf{r}_2)\rangle$. The average is taken with respect to the ensemble and $\mathbf{r}_1$, $\mathbf{r}_2$. Note that $f_{\mathrm{m2}}(\phi) > f_{\mathrm{m1}}(\phi)$ at all ϕ.

For the osmotic compressibility $P(\phi)$, we employ the Ohta–Oono semiempirical formula [5,6]:

$$P(\phi) = 1 + \frac{1}{2}X\exp\{0.3089[X^{-1} + (1 - X^{-2})\ln(1+X)]\} \tag{23}$$

with $X \equiv 3.49\phi/\phi^*$. Here ϕ^* is the overlap monomer density defined by $\phi^*(2^{1/2}R_{\mathrm{g0}})^3 = Na^3$, where a^3 is the monomer volume. We evaluate $\langle\Delta\phi(\mathbf{r}_1)\Delta\phi(\mathbf{r}_2)\rangle$ for bulk solution of the average monomer density ϕ. See Ref. [4] for details.

For the one-dimensional unperturbed eigenvalues ϵ_{0k}, we employ the values obtained for an athermal chain in the slit geometry. We also take into account the chain contraction and concomitant decrease in the confinement entropy. As we did for the confinement by the slit, we introduce a Gaussian-equivalent radius of gyration R_{gG} so that the Gaussian chain with R_{gG} and the athermal chain with R_{g} experience the same confinement entropy [10]. With R_{gG}, ϵ_{0k} given as:

$$N\epsilon_{0k} = (k\pi R_{\mathrm{gG}}/d)^2 \tag{24}$$

enters Eq. (12). We allow chain contraction and employ the contraction factor $R_{\mathrm{g}}/R_{\mathrm{g0}}$ found for unconfined solutions as we did in the slit geometry [10].

The chemical potential μ_{I} of the confined chain is calculated from the insertion probability (Eq. (15)). In the first-order approximation,

$$(\mu_{\mathrm{I}} - \mu^{\mathrm{o}})/k_{\mathrm{B}}T = \ln \phi_{\mathrm{AV}} - \ln\left(\left(\frac{8}{\pi^2}\right)^2 \sum_{k,l:\mathrm{odd}} b_{kl}^2 \exp(-N\epsilon_{kl})\right) \tag{25}$$

where μ^{o} is the chemical potential at some reference state, and ϕ_{AV} is the average monomer density in the channel. In the second-order approximation [4],

$$\begin{aligned}(\mu_{\mathrm{I}} - \mu^{\mathrm{o}})/k_{\mathrm{B}}T &= \ln \phi_{\mathrm{AV}} - \ln\left(\left(\frac{8}{\pi^2}\right)^2 \sum_{k,l:\mathrm{odd}} b_{kl}^2 \exp(-N\epsilon_{kl})\right) \\ &\quad - \ln(\cos(h(\phi)))\end{aligned} \tag{26}$$

where we evaluate $h(\phi)$ at the center of the channel. The last term accounts for second-order correction to μ due to the density fluctuations. The chemical potential μ_{E} of the chain in the bulk solution at concentration ϕ_{E} is given as, common to the two approximations,

$$\begin{aligned}(\mu_{\mathrm{E}} - \mu^{\mathrm{o}})/k_{\mathrm{B}}T &= \ln \phi_{\mathrm{E}} + P(\phi_{\mathrm{E}}) - 1 + \int_0^{\phi_{\mathrm{E}}} [P(\varphi) - 1]\varphi^{-1}\,\mathrm{d}\varphi\end{aligned} \tag{27}$$

Equating μ_{I} to μ_{E} gives the partition coefficient $K = \phi_{\mathrm{AV}}/\phi_{\mathrm{E}}$.

The eigenequation (Eq. (11)) is solved self-consistently. Thus, the confined solution system is specified by R_{g0}/d and $\phi_{\mathrm{AV}}/\phi^*$ only.

3. Simulation method

Monte Carlo simulation was performed on a cubic lattice. Details of the simulation method is explained elsewhere [8]. Briefly, chains with $N = 100$ and 500 monomers were generated. Their radii of gyration in the dilute bulk solution are 6.524 and 16.78, respectively, where the unit length is the lattice spacing. Their overlap monomer densities are 0.1164 and 0.0361, respectively. The monomer density profile was obtained in a simulation box consisting of a channel space only. The size of the box was $L_x \times L_y \times 150$, where $L_x = L_y$ was varied. A periodic boundary condition was applied in the z direction. The walls are at $x = 0$, $x = L_x + 1$, $y = 0$, and $y = L_y + 1$. The channel width is $d_{\mathrm{sim}} = L_x + 1$ in the simulation. The density $\phi(x, y)$ is defined as the average of the ratio of the occupied sites to the available sites at (x, y). The partition coefficient was evaluated in another simulation box that consists of the channel space and the surrounding free space connected to the channel through its mouths. The box size was $L_x \times L_y \times 50$ for the channel and $50 \times 50 \times 50$ for the exterior space. Chains were moved according to the reptation moves and the Metropolis rule. Typically trial moves as many as 4×10^{10} were needed to obtain a smooth profile. The computing was done on a super computer.

We take a few precautions [4] to compare the simulation results obtained for a channel with a cross section of $d_{\mathrm{sim}} \times d_{\mathrm{sim}}$ and the theoretical results obtained for a channel of $d \times d$ in the continuum. First, the simulation data are obtained at discrete points on the lattice only, and the average density $\phi_{\mathrm{AV,sim}}$ is calculated for these points. For comparison, the theory calculates the density at the coordinates of the lattice points. The partition coefficient K_{sim} is thus obtained as $K_{\mathrm{sim}} = \phi_{\mathrm{AV,sim}}/\phi_{\mathrm{E}}$. The exterior solution does not need this correction. Second, the monomer density near the wall in the lattice simulation slightly deviates from the scaling-law prediction, $\phi(x) \sim x^{1/\nu}$ with $\nu = 0.59$ [11–13]. To coerce the scaling law, we need to add a positive constant γ to x: $\phi(x) \sim (x + \gamma)^{1/\nu}$ [14]. In effect, monomers perceive the theoretical wall somewhat behind the physical wall sitting on the lattice points. Our detailed simulation study [15] estimated $\gamma \cong 0.13$ at low concentrations in a weak confinement and $\gamma \cong 0.36$ in the semidilute solutions. We employ $\gamma = 0.36$ throughout this article.

4. Calculation results

In this section, we will show the results obtained with $f_{\mathrm{m2}}(\phi)$ only. The difference between $f_{\mathrm{m1}}(\phi)$ and $f_{\mathrm{m2}}(\phi)$ will be discussed when we compare the calculation results with the simulation results.

Fig. 1 shows the leading eigenvalues $N\epsilon_{ij}$ ($1 \le i \le j \le 5$; i, j: odd) of Eq. (11) as a function of $\phi_{\mathrm{AV}}/\phi^*$. Results for a weak confinement ($R_{\mathrm{g0}}/d = 0.1$) and a strong confinement ($R_{\mathrm{g0}}/d = 0.5$) are shown. At low concentrations, the interactions are absent, and the matrix in the eigenequation is diagonal. Its diagonal elements $(\pi R_{\mathrm{gG}}/d)^2(i^2 + j^2)$ are the eigenvalues. In the figure, $N\epsilon_{11}$, $N\epsilon_{31}$, $N\epsilon_{33}$, $N\epsilon_{51}$, $N\epsilon_{53}$, and $N\epsilon_{55}$ in the low concentration limit are proportional to 2, 10, 18, 26, 34, and 50, respectively. The two sets for $R_{\mathrm{g0}}/d = 0.1$ and 0.5 are evenly displaced by about 33,

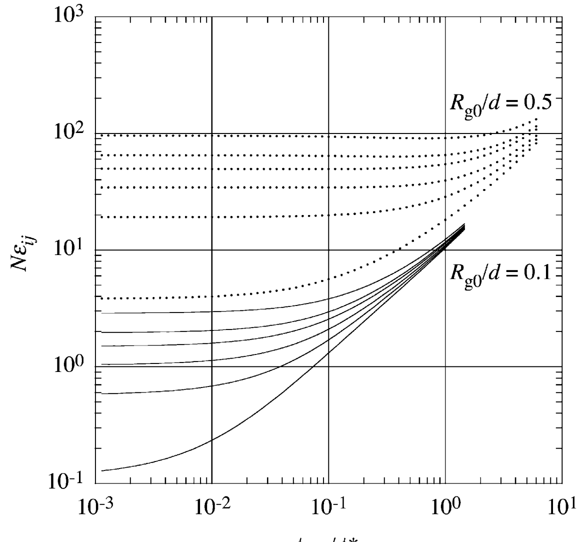

Fig. 1. Leading eigenvalues $N\epsilon_{11}$, $N\epsilon_{31}$, $N\epsilon_{33}$, $N\epsilon_{51}$, $N\epsilon_{53}$, and $N\epsilon_{55}$ (from bottom to top) plotted as a function of ϕ_{AV}/ϕ^*. Results for a weak confinement ($R_{g0}/d = 0.1$; solid lines) and a strong confinement ($R_{g0}/d = 0.5$; dotted lines) are shown.

close to $(0.5/0.1)^2$. The small difference is due to the adoption of the Gaussian equivalent radius to give an appropriate confinement entropy to an excluded-volume chain. With an increasing ϕ_{AV}/ϕ^*, the eigenvalues with lower indices climb, whereas the eigenvalues with higher indices are held more or less unchanged, erasing the difference between $N\epsilon_{ij}$. Eventually, $N\epsilon_{ij}$ of different indices increase in unison. In the stronger confinement, a higher ϕ_{AV} is needed for the eigenvalues to start to increase, because the interactions are the smaller part of the matrix elements until ϕ_{AV} becomes comparable to ϕ^*. We see a decrease in $N\epsilon_{33}$, $N\epsilon_{51}$, $N\epsilon_{53}$, and $N\epsilon_{55}$ at $\phi_{AV}/\phi^* < 1$, ascribed to the chain contraction that decreases $(\pi R_{gG}/d)^2(i^2 + j^2)$. The trends are similar to those we observed in the slit geometry [4].

Examples of the two-dimensional density profile $\phi(x, y)$ are shown in Fig. 2 for $R_{g0}/d = 0.5$. Three parts of the figure were obtained at $\phi_{AV}/\phi^* =$ (a) 0.1, (b) 1, and (c) 5.275. In (a), the density profile is dominated by the ground state ($k = l = 1$; $i = j = 1$), $\sin^2(\pi x/d)\sin^2(\pi y/d)$. The density falls off toward zero at the walls as x^2 near the wall of $x = 0$, for instance. The depletion at the walls becomes smaller with an increasing ϕ_{AV}. In (c), the profile has a plateau at the center.

Fig. 3 shows the partition coefficient K as a function of ϕ_E/ϕ^*, the monomer density ϕ_E in the surrounding solution reduced by ϕ^*. The plot is given for different chain dimensions, R_{g0}/d. As in the slit, K exhibits a diffuse transition from a weak penetration to a strong penetration with an increasing ϕ_E/ϕ^*, although it is less diffuse and requires a higher ϕ_E/ϕ^* in the channel than in the slit [4]. The transition requires a higher ϕ_E/ϕ^* for more strongly confined chains.

We now take another look at the same data. In Fig. 4, we plot K as a function of ϕ_E for a given channel width d. For this purpose, we use the definition of ϕ^*, $\phi^* R_{g0}^3 \cong Na^3$. Because $N \cong (R_{g0}/a)^{1/\nu} = (R_{g0}/a)^{1.695}$, $\phi_E \sim (\phi_E/\phi^*)(R_{g0}/d)^{1/\nu-3} = (\phi_E/\phi^*)(R_{g0}/d)^{-1.305}$ is used for the abscissa. It is obvious that, with an increasing chain length, the plot approaches an asymptotic curve (not shown) that rises sharply from zero at around $(\phi_E/\phi^*)(R_{g0}/d)^{-1.305} = 2$. Plots for different chain lengths overlap with the asymptotic curve at high concentrations. Apparently, the partitioning at high concentrations does not depend on the chain length, but is determined by ϕ_E only. This fact substantiates the view that the partitioning of the semidilute solution is based on the blob size (= correlation length) relative to the channel width [16], just as the partitioning of the dilute solution is governed by R_{g0}/d.

As discussed in our preceding article on simulations [8], the partition coefficient K of polymer chains with a channel follows roughly the square of the partition coefficient K_S of the same chains with a slit of the same wall-to-wall distance d, compared at the same ϕ_E, when the confinement is weak. We compare K (solid lines) with K_S^2 (dashed lines) for $R_{g0}/d = 0.2$, 0.5, and 1 in Fig. 5. We used $f_{m2}(\phi)$ to calculate K_S. In the low concentration limit, $K = K_S^2$, because confinement of the Gaussian chain is independent in each direction in the absence of interactions. With an increasing ϕ_E, the solid line runs away from the dashed line. The discrepancy

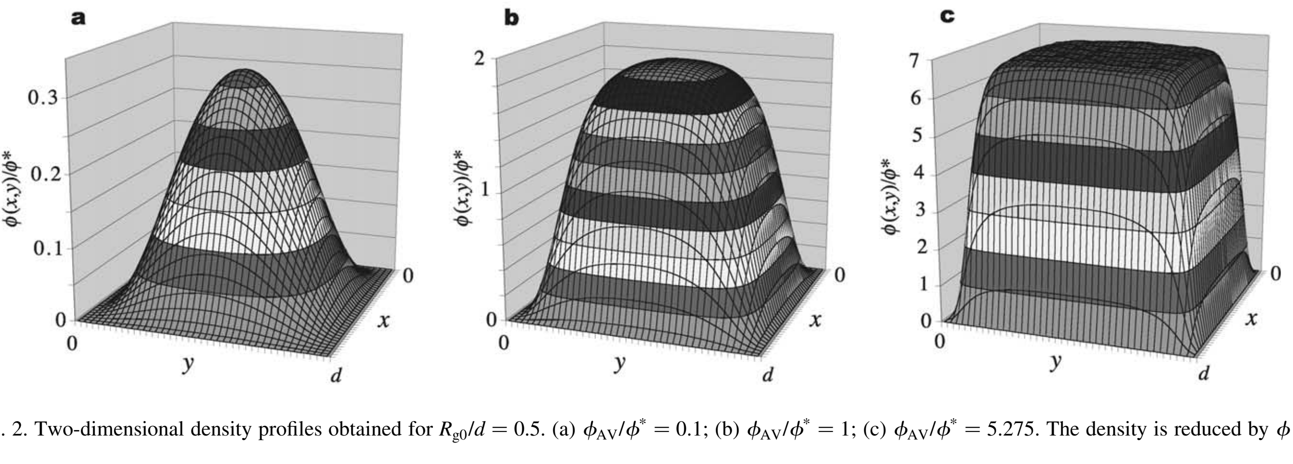

Fig. 2. Two-dimensional density profiles obtained for $R_{g0}/d = 0.5$. (a) $\phi_{AV}/\phi^* = 0.1$; (b) $\phi_{AV}/\phi^* = 1$; (c) $\phi_{AV}/\phi^* = 5.275$. The density is reduced by ϕ^*.

between K and K_S^2 is more serious in the stronger confinement, especially when the correlation length ξ in the exterior solution is not sufficiently small compared with d. Until ξ becomes sufficiently smaller than d, entrance into the channel is much more difficult compared with entrance into the slit. At higher concentrations, closeness of K to K_S^2 is regained, as ξ becomes sufficiently short. A similar trend was observed in our previous simulation studies [8].

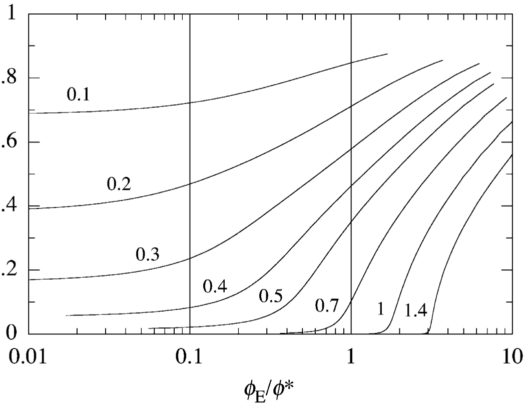

Fig. 3. Partition coefficient K plotted as a function of ϕ_E/ϕ^* in the surrounding solution. The value of R_{g0}/d is indicated adjacent to each curve.

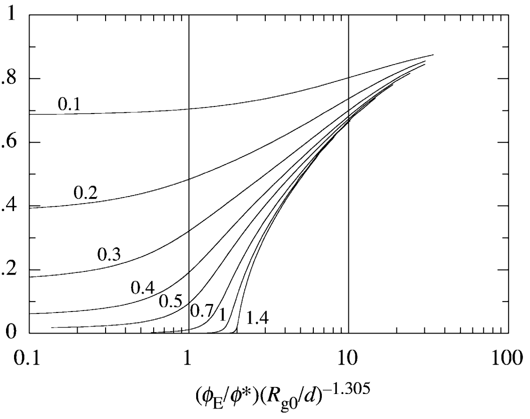

Fig. 4. Partition coefficient K plotted as a function of $\phi_E \sim (\phi_E/\phi^*)(R_{g0}/d)^{-1.305}$. See text for definition of the quantity on the abscissa. The chain dimension is indicated next to each curve.

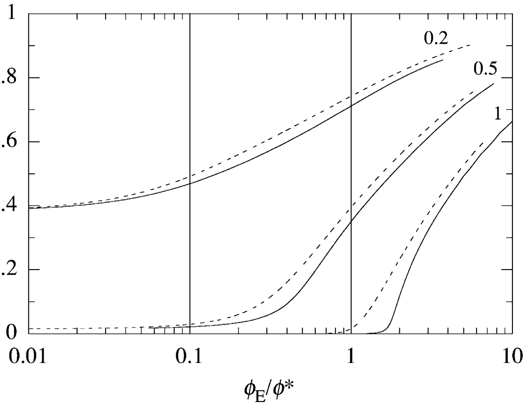

Fig. 5. Partition coefficient for chains of R_{g0} with a square channel (solid line) is compared with the square of the partition coefficient with a slit of the same wall-to-wall distance d (dashed line). Three chain dimensions, $R_{g0}/d = 0.2$, 0.5, and 1, are compared.

5. Comparison with simulation results

It is not easy to visually compare the two-dimensional density profile $\phi(x, y)$ between theory and simulation. Therefore, we select line profiles at two longitudinal

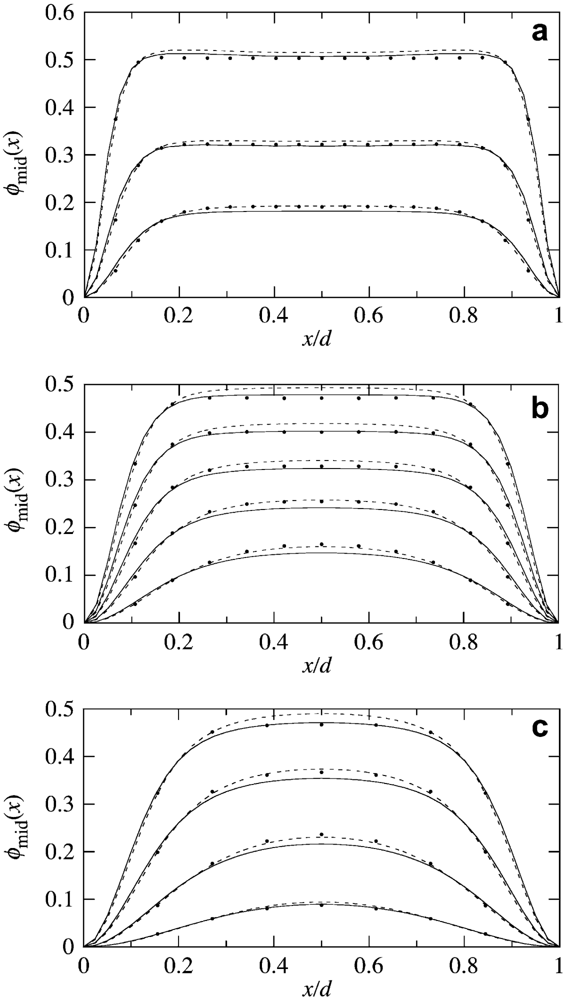

Fig. 6. Comparison of the density profile $\phi_{mid}(x)$ along the midplanes of the channel. The dots are from simulation for $N = 100$, the solid lines are from the theory with f_{m2}, and the dashed lines with f_{m1}. (a) $d_{sim} = 20$, $\phi_{AV,sim} = 0.1385$, 0.277, 0.4737 from bottom to top. (b) $d_{sim} = 12$, $\phi_{AV,sim} = 0.08264$, 0.16528, 0.24792, 0.3306, 0.4132. (c) $d_{sim} = 8$, $\phi_{AV,sim} = 0.0408$, 0.1224, 0.2449, and 0.3677. The lines were obtained for $R_{g0}/d_{sim} =$ (a) 0.3262, (b) 0.5437, and (c) 0.8155.

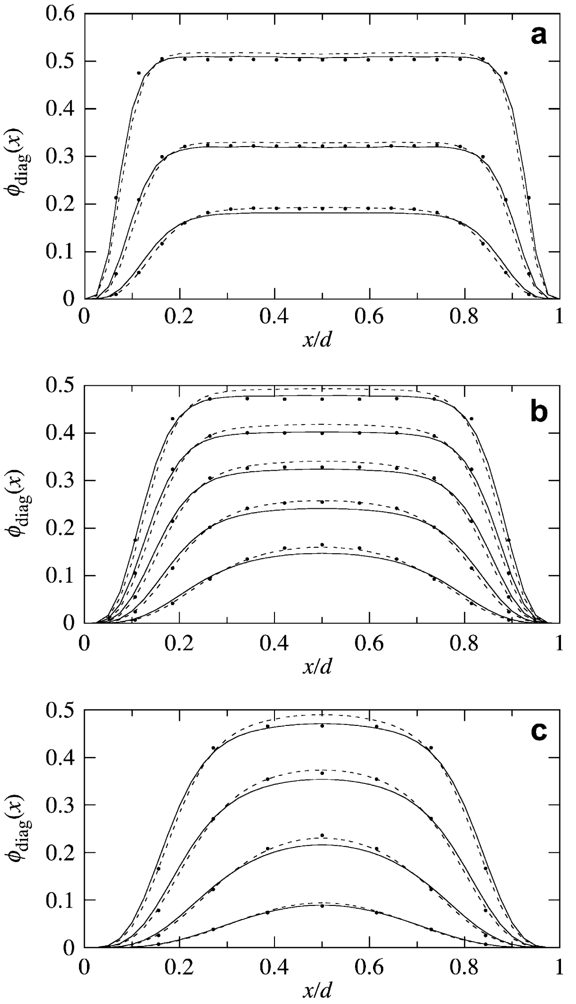

Fig. 7. Comparison of the density profile $\phi_{\mathrm{diag}}(x)$ along the diagonal planes of the channel. The data were obtained for the same sets as those in Fig. 6.

cross sections of the channel. One is $\phi_{\mathrm{mid}}(x) = [\phi(x, d/2) + \phi(d/2, x)]/2$, the density along the midplanes of the channel. The other is $\phi_{\mathrm{diag}}(x) = [\phi(x, x) + \phi(x, d - x)]/2$ along the diagonal planes. Fig. 6(a), (b) and (c) compares $\phi_{\mathrm{mid}}(x)$ for the chains of $N = 100$ in a channel of $d_{\mathrm{sim}} = 20$, 12, and 8, respectively, at several values of $\phi_{\mathrm{AV,sim}}$. Calculations were done for $\phi^* = 0.1164$ and $R_{\mathrm{g0}}/d_{\mathrm{sim}} = 0.3262$, 0.5437, and 0.8155, respectively. Fig. 7(a), (b) and (c) compares $\phi_{\mathrm{diag}}(x)$ for the same confined solutions. The solid lines were obtained with $f_{\mathrm{m2}}(\phi)$ and the dashed lines with $f_{\mathrm{m1}}(\phi)$. The profiles obtained in the simulations, shown as dots, are the averages of the profiles at x and $d - x$.

The two profiles are a one-dimensional cut of the two-dimensional profile. There may be a systematic deviation between the two theoretical profiles and the simulation profile. For instance, $\phi_{\mathrm{mid}}(x)$ for $d_{\mathrm{sim}} = 12$ at $\phi_{\mathrm{AV,sim}} = 0.08264$ has more points of simulation data above the solid line than those below the curve. The imbalance can occur because there are more points that have the same x near the wall than there are near the center.

The two profiles are approximately related by $\phi_{\mathrm{diag}}(x)/\phi_{\mathrm{peak}} = [\phi_{\mathrm{mid}}(x)/\phi_{\mathrm{peak}}]^2$, where ϕ_{peak} is the density at the center of the channel cross section [8]. As a result, the depletion layer in $\phi_{\mathrm{diag}}(x)$ is 60 to 70% thicker than the one in $\phi_{\mathrm{mid}}(x)$.

For the three channel widths, the simulation data are close to the dashed lines at $\phi_{\mathrm{AV,sim}} < 0.2$, but at higher ϕ_{AV}, the solid lines run close to the simulation data. In $d_{\mathrm{sim}} = 8$, the dashed lines give a better fit except for the highest $\phi_{\mathrm{AV,sim}}$. Note that a strong potential spreads the monomer density toward the walls at high concentrations, overcoming the entropy penalty near the walls and thus thinning the depletion layer. The comparison tells that the interactions of the chains follow closely f_{m1} until ϕ_{AV} becomes sufficiently high. Recall that f_{m2}, not f_{m1}, gave a good agreement with the simulation profiles in the slit geometry in different confinement strengths over a wide range of ϕ_{AV} [4]. We consider the difference in the theory's capability to predict the simulation profiles between the slit and channel geometries is meaningful and caused by the difference of interactions in the two geometries. In solutions within the channel, especially under strong confinement, the chains are packed along the channel rather uniformly. The correlation in the monomer density fluctuations is cut off at distance d. In the slit, the correlation extends beyond d, although it is weaker compared with the bulk solution. Thus, the fluctuations in the monomer density in the channel are smaller compared with the bulk solution or in the two-dimensional slit geometry, especially at around ϕ^* of the bulk solutions. Therefore, f_{m1} obtained by assuming a uniform monomer density in the bulk describes rather well the density profiles. As the correlation length in the solution confined to the channel decreases to a value sufficiently smaller than the channel width, the solution behaves rather three-dimensionally. Then it becomes necessary to take into account the local monomer density fluctuations, and $f_{\mathrm{m2}}(\phi)$ gives a better description of the confined solution.

Interestingly, the simulation profiles at higher concentrations exhibit a caldera pattern with a shallow basin at the center. It is more pronounced compared with the one observed in the slit geometry [4]. The theoretical curves reproduce the pattern to some extent (see Figs. 6(a) and 7(a)). The shallow basin at the center is due to suppression of higher-order modes. The thinning of the depletion later at the walls with an increasing ϕ_{AV} is made possible through enhancement of the higher-order modes, but the remaining depletion places a cap on the mode order and keeps the modes with a higher order from growing. As a result, the sharp rise in $\phi(x, y)$ near the wall is accompanied by a slight decline in $\phi(x, y)$ in the hinterland.

The partition coefficient K_{sim} is compared in Fig. 8 for $N = 100$, $d_{\mathrm{sim}} = 20$; $N = 100$, $d_{\mathrm{sim}} = 8$; and $N = 500$, $d_{\mathrm{sim}} = 8$. The solid lines were obtained with f_{m2} and the dashed lines with f_{m1}. The agreement and disagreement between the theoretical curves and the simulation data are parallel to those we have seen in the profiles plot. When the

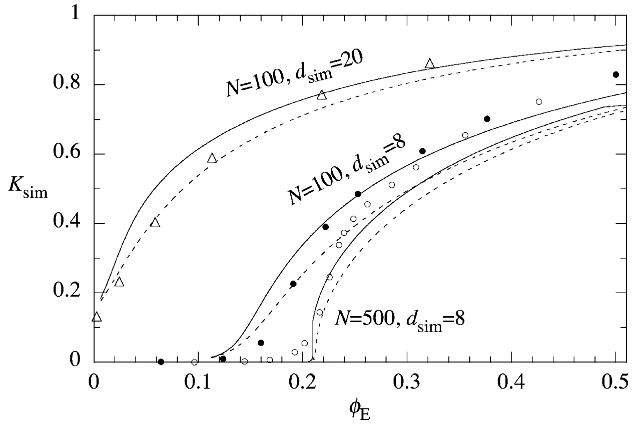

Fig. 8. Comparison of the partition coefficient K_{sim}, plotted as a function of ϕ_{E}. Triangles, closed circles, and open circles were obtained in simulations with $N = 100$, $d_{\mathrm{sim}} = 20$; $N = 100$, $d_{\mathrm{sim}} = 8$; and $N = 500$, $d_{\mathrm{sim}} = 8$, respectively. The lines (solid lines for f_{m2} and dashed lines for f_{m1}) are from theory for $R_{\mathrm{g0}}/d_{\mathrm{sim}} = 0.3262$, $\phi^* = 0.1164$; $R_{\mathrm{g0}}/d_{\mathrm{sim}} = 0.8155$, $\phi^* = 0.1164$; and $R_{\mathrm{g0}}/d_{\mathrm{sim}} = 2.098$, $\phi^* = 0.0361$.

confinement is weak, f_{m1} gives a good agreement with the simulation data up to $\phi_{\mathrm{E}} \cong 0.2$. Beyond that ϕ_{E}, f_{m2} is better. In the stronger confinement, the theory cannot describe the simulation results except at around $\phi_{\mathrm{E}} =$ 0.2–0.25 by f_{m2}. The discrepancy between theory and simulation is greater in this plot compared with the profiles plot. This comparison points to the sensitivity of the partition coefficient. The latter depends on a delicate balance of the interaction with the confinement entropy.

A downward deviation of the theoretical K_{sim} at high concentrations is evident, especially in the strong confinement. Simulated chains find it much easier to enter the channel compared with the theory at high concentrations. The discrepancy may be due to the strong contraction of the chains at higher concentrations in the narrow channel. The latter will facilitate the entrance. In our calculation, we used the three-dimensional chain contraction factor. It is an overestimate (chains in the channel do not contract as much) below the overlap monomer density within the channel that is about 0.10 in $d_{\mathrm{sim}} = 8$ for both $N = 100$ and 500, but is an underestimate when the chains are congested in the channel.

There is a stepwise increase at $\phi_{\mathrm{E}} \cong 0.21$ in the solid line for $N = 500$, $d_{\mathrm{sim}} = 8$. The first-order transition-like increase is due to the presence of two phases in the solution of strongly confined chains. In a certain range of ϕ_{AV}, a dilute solution of extended chains and a semidilute solution of contracted chains coexist. The two-phase regime is, however, artificially caused by our assumption that chains confined to a channel experience the same contraction as in the unconfined solution. A single chain in a strong confinement has already a high local concentration. Its monomer density is $N/(d^2R_{\|})$, where $R_{\|}$ is the dimension of the single chain along the channel. The chain does not show contraction until ϕ_{AV} reaches $N/(d^2R_{\|})$. Therefore, the simulation results do not exhibit a stepwise increase in K_{sim}.

6. Conclusions

We have presented a mean-field Gaussian chain theory for non-dilute polymer solutions confined to a square channel. A good agreement with the simulation results was obtained when the first- and second-order mean field potentials were used at low and high concentrations, respectively. A small difference in the partition coefficient between theory and simulation indicates a need to study the contraction of chains strongly confined to a narrow channel. The investigation is currently under way.

The theory confirms the unique penetration transition characteristic of narrow channels and long chains, which is absent in slits. This transition may find its use in separation techniques for macromolecules such as high osmotic pressure chromatography [17].

Extension of our theory to a cylindrical geometry will be easy, because the monomer density depends only on the radial distance from the cylinder axis even at high concentrations. The problem is essentially one-dimensional. Computation will be fast even for weakly confined chains that require many modes to follow the flat profile with fidelity.

Acknowledgements

Financial support from NSF under DMR-9876360 and Slovak Academy of Sciences (SAS) under 2/7076/21 is acknowledged. Usage of computational resources of Computer Center of SAS is acknowledged.

Appendix A. Computation of eigenequation

To facilitate numerical solution of the eigenequation on computer, we index the pair of mode numbers (k, l) into a compound mode number L. We introduce L by $L \equiv k(k-1)/2 + l$ with $k \geq l \geq 1$ for odd k and l. Conversely, we can restore (k, l) from L. When the upper limit of k is set to $k_{\max}$ in computation, then $1 \leq L \leq L_{\max} = k_{\max}(1 + k_{\max})/2$. It is necessary to choose a sufficiently large $k_{\max}$ to express the detailed spatial variation of the monomer density in the channel. Because $\epsilon_{kl} = \epsilon_{lk}$ and $u_{kl}(x, y) = u_{lk}(y, x)$, Eq. (A1) is written as:

$$G_{xy}(x, y; x', y'; n) = \sum_{L=1}^{L_{\max}} [u_L(x, y)u_L(x', y') + (1 - \delta_{kl})u_L(y, x)u_L(y', x')]\exp(-n\epsilon_L) \quad \text{(A1)}$$

Note that $u_{kl}(x, y)$ with $k > l$ represents a higher-order mode in the x direction compared with the y direction. Therefore, $a_{klij} = 0$ for $k > l$ and $i < j$. Because the non-zero elements of a_{klij} are restricted to $i \geq j$, we can use another compound index I to represent (i, j) as $I = i(i-1)/2 + j$ for odd i, j. The maximum of I is $L_{\max}$. Eq. (A2) is now

$$u_L(x,y) = \sum_{I=1}^{L_{\max}} a_{LI} u_{0i}(x) u_{0j}(y) \qquad (L = 1, 2, \ldots, L_{\max}) \tag{A2}$$

The eigenequation now looks familiar:

$$\mathbf{M}\mathbf{a}_L = (N\epsilon_L)\mathbf{a}_L \tag{A3}$$

The two-dimensional matrix $\mathbf{M}$ is of size $L_{\max} \times L_{\max}$:

$$M_{II'} = N(\epsilon_{0i} + \epsilon_{0j})\delta_{II'} + U_{II'} \qquad (I, I', \ldots, L_{\max}) \tag{A4}$$

with

$$U_{II'} = \int_0^d \int_0^d u_{0i}(x) u_{0j}(y) f(\phi(x,y)) u_{0i'}(x) u_{0j'}(y) \mathrm{d}x\, \mathrm{d}y \tag{A5}$$

where I' represents (i', j').

The insertion probability p is now

$$p = d^{-2} \int_0^d \mathrm{d}x' \int_0^d \mathrm{d}x'' \int_0^d \mathrm{d}y' \int_0^d \mathrm{d}y'' G_{xy}(x', y'; x'', y''; N)$$

$$= (8/\pi^2)^2 \sum_{L=1}^{L_{\max}} b_L^2 (2 - \delta_{kl}) \exp(-N\epsilon_L) \tag{A6}$$

where

$$b_L = \sum_{I=1}^{L_{\max}} (i\,j)^{-1} a_{LI} \tag{A7}$$

The density profile is now

$$\phi(x,y) = \frac{\phi_{\mathrm{AV}}}{p}\left(\frac{8d}{\pi^2}\right)^2 \sum_{J=1}^{L_{\max}} \sum_{J'=1}^{L_{\max}} c_{JJ'}[u_{0j}(x)u_{0m}(y) + (1-\delta_{jm})u_{0m}(x)u_{0j}(y)] \times [u_{0j'}(x)u_{0m'}(y) + (1-\delta_{j'm'})u_{0m'}(x)u_{0j'}(y)] \tag{A8}$$

where $c_{JJ'}$ is symmetric:

$$c_{JJ'} = \sum_{L=1}^{L_{\max}} b_L a_{LJ} \sum_{L'=1}^{L_{\max}} b_{L'} a_{L'J'} e_{LL'} \tag{A9}$$

with

$$e_{LL'} = \begin{cases} \exp(-N\epsilon_L) & L = L' \\ \dfrac{\exp(-N\epsilon_{L'}) - \exp(-N\epsilon_L)}{N(\epsilon_L - \epsilon_{L'})} & L \neq L' \end{cases} \tag{A10}$$

Note that the summations in Eq. (A9) are for $k \geq l$ and $k' \geq l'$ only, because $c_{JJ'}$ is defined for $i \geq j$ and $i' \geq j'$, and $a_{klij} = 0$ for $k < l$ and $i \geq j$.

References

[1] Daoud M, de Gennes PG. J Phys (Paris) 1977;38:85.
[2] de Gennes PG. Scaling concepts in polymer physics. Ithaca: Cornell Univ. Press, 1979.
[3] Brazhnik PK, Freed KF, Tang H. J Chem Phys 1994;101:9143.
[4] Teraoka I, Wang Y. J Chem Phys 2001;115:1105.
[5] Ohta T, Oono Y. Phys Lett 1982;89A:460.
[6] Oono Y. Adv Chem Phys 1985;61:301.
[7] Teraoka I, Cifra P. J Chem Phys 2001;115:11362.
[8] Cifra P, Teraoka I. Polymer 2002;43:2409.
[9] Casassa EF, Tagami Y. Macromolecules 1969;2:14.
[10] Wang Y, Teraoka I. Macromolecules 2000;33:3478.
[11] Eisenriegler E. Phys Rev E 1997;55:3116.
[12] Milchev A, Binder K. Euro Phys J 1998;B3:477.
[13] Milchev A, Binder K. Euro Phys J 2000;B13:607.
[14] De Joannis J, Jimenez J, Rajagopalan R, Bitsanis I. Euro Phys Lett 2000;51:41.
[15] Teraoka I, Cifra P, Wang Y. Macromolecules 2001;34:7121.
[16] Wang Y, Teraoka I. Macromolecules 1997;30:8473.
[17] Teraoka I. In: Wu CS, editor. Column handbook for size exclusion chromatography. San Diego: Academic Press, 1999.